JACS
JOURNAL OF THE AMERICAN CHEMICAL SOCIETY
Article
pubs.acs.org/JACS

Transition Metal Nitride Coated with Atomic Layers of Pt as a Low-Cost, Highly Stable Electrocatalyst for the Oxygen Reduction Reaction

Xinlong Tian,[†] Junming Luo,[†] Haoxiong Nan,[†] Haobin Zou,[†] Rong Chen,[†] Ting Shu,[†] Xiuhua Li, Yingwei Li,[†] Huiyu Song, Shijun Liao,*[,†] and Radoslav R. Adzic*[,‡]

[†]The Key Laboratory of Fuel Cell Technology of Guangdong Province & the Key Laboratory of New Energy Technology of Guangdong Universities, School of Chemistry and Chemical Engineering, South China University of Technology, Guangzhou 510641, China

[‡]Chemistry Department, Brookhaven National Laboratory, Upton, New York 11973, United States

Supporting Information

ABSTRACT: The main challenges to the commercial viability of polymer electrolyte membrane fuel cells are (i) the high cost associated with using large amounts of Pt in fuel cell cathodes to compensate for the sluggish kinetics of the oxygen reduction reaction, (ii) catalyst degradation, and (iii) carbon-support corrosion. To address these obstacles, our group has focused on robust, carbon-free transition metal nitride materials with low Pt content that exhibit tunable physical and catalytic properties. Here, we report on the high performance of a novel catalyst with low Pt content, prepared by placing several layers of Pt atoms on nanoparticles of titanium nickel binary nitride. For the ORR, the catalyst exhibited a more than 400% and 200% increase in mass activity and specific activity, respectively, compared with the commercial Pt/C catalyst. It also showed excellent stability/durability, experiencing only a slight performance loss after 10 000 potential cycles, while TEM results showed its structure had remained intact. The catalyst's outstanding performance may have resulted from the ultrahigh dispersion of Pt (several atomic layers coated on the nitride nanoparticles), and the excellent stability/durability may have been due to the good stability of nitride and synergetic effects between ultrathin Pt layer and the robust TiNiN support.

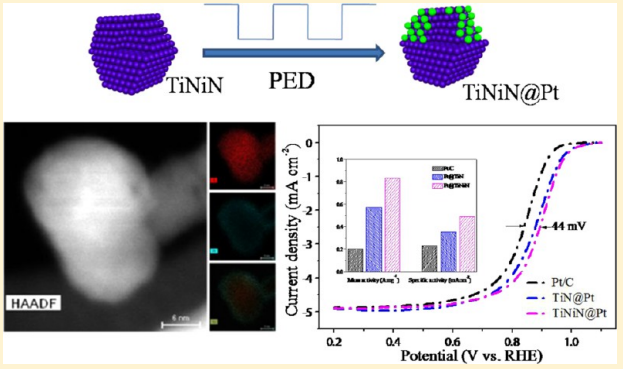

1. INTRODUCTION

Low-temperature polymer electrolyte membrane fuel cells (PEMFCs) have attracted tremendous attention as promising power sources for transportation and residential applications because they generate no harmful emissions and have high-energy conversion efficiency.[1−4] However, the development of PEMFCs is severely hampered by the sluggish kinetics of the oxygen reduction reaction (ORR), as well as the use of platinum (Pt) as the electrocatalyst, whose scarcity makes it costly.[5−8] The design and fabrication of inexpensive, highly active, and stable ORR catalysts is therefore extremely important, but it remains challenging. A number of methods have been proposed for exploring new electrocatalysts with low Pt loadings, including alloying Pt with secondary transition metals,[9−11] depositing atomic layers of Pt onto other fine metal particles to create core−shell structures,[12−15] and employing various dealloying approaches.[16,17] Specially, the core−shell structure with a thin Pt shell around the core not only minimizes Pt use and maximizes the exposure of Pt to oxygen, but also introduces the expected core−shell interactions that enable the tuning of both electronic and surface strain effects for optimal catalysis.[12,18]

Although recent studies have greatly improved catalyst performance, the core elements are still costly metals, such as Pd,[13,19−21] Au,[22] Ir,[23−25] and Ru.[26,27] In addition, carbon black is still the most widely used electrocatalyst support for the ORR; yet corrosion of the carbon support by electrochemical oxidation under fuel cell operating conditions causes the precious metals to aggregate and separate from the carbon support, with consequent performance degradation having been extensively reported.[28−33] Hence, these catalysts have high precious metal content and poor durability, as harsh oxidation conditions decrease their electrochemical surface area (ECSA) and the resultant fuel cell performance. What is needed instead are highly active, stable, and low-cost cathode electrocatalysts.

Recently, transition metal nitrides (TMNs) have been explored as ideal candidates for replacing noble metal catalyst supports in PEMFCs because TMNs are highly electrically

Received: October 30, 2015
Published: January 21, 2016

DOI: 10.1021/jacs.5b11364
J. Am. Chem. Soc. 2016, 138, 1575−1583

conductive (metallic), thermally stable with exceptional hardness (covalent), and corrosion resistant under fuel cell operating conditions.[2,34−37] They also affect the electrocatalytic activity of the supported noble metals due to metal−support interactions. Catalysts composed of Pt on TMN materials (Pt/TMNs) have been reported to exhibit better ORR performance and durability than commercial Pt/C.[38−41] It is believed that Pt/TMN catalysts exhibit strong metal−support interactions (SMSI) and therefore the Pt nanoparticles (NPs) adhere to the support more strongly than they would to a carbon support, facilitating both stability and electron transfer during the catalysis process. Based on the above considerations, one would expect to be able to assemble a TMN@Pt catalyst with a core−shell structure that would exhibit the desirable catalytic qualities of both core−shell and TMN-supported Pt catalysts, that is, combining the merits of the Pt shell's high activity and the low cost and superb stability of core TMN NPs.

Herein, we report on TiNiN@Pt catalyst, which was prepared by nitriding an ammonia complex of Ti and Ni at 700 °C in a NH_3 atmosphere, then using a pulse deposition method to deposit a Pt shell several atomic layers thick on the resulting TiNiN NPs. We posited that such an approach would solve the problems of low catalyst utilization and degradation due to carbon-support corrosion, while also achieving high catalytic activity with low Pt loading. The catalyst exhibited surprisingly high activity and superior stability for the ORR in the acidic solution. The mass activity was up to 0.83 A mg^{-1}_{Pt} at 0.9 V, which was four times that of the commercial carbon-supported Pt catalyst (20 wt % Pt on Vulcan XC-72R, JM Pt/C).

2. EXPERIMENTAL PROCEDURES

2.1. Synthesis of Nitride Nanoparticles. TMN NPs were prepared by a complexation−nitridation approach. For example, to prepare $Ti_{0.95}Ni_{0.05}N$ (abbreviated as TiNiN), titanium tetrachloride ($TiCl_4$, 1 mL) and nickel acetatetetrahydrate (Ni $(CH_3COO)_2{\cdot}4H_2O$, 0.119 g) were dissolved in 30 mL of ethanol under stirring. Next, NH_3 gas was introduced to the solution (at a rate of 30 sccm) under continuous stirring for 30 min, yielding a precipitate of the complex. After that, the mixture was transferred to a vacuum drying oven and kept at 80 °C overnight to evaporate the ethanol solvent. The complex powder was placed in a tubular furnace and nitrided at 700 °C under an NH_3 gas flow (50 sccm) for 2 h, and then the sample was cooled to room temperature under the protection of an argon gas flow. For comparison, TiN NPs were synthesized using the same processes but without the addition of Ni $(CH_3COO)_2{\cdot}4H_2O$ in the precursor.

2.2. Preparation of TMN@Pt Catalyst. An extra-thin Pt layer was deposited on the TMN NPs using a pulse electro deposition (PED) process developed by our group.[22,24,42] For this, 5 mg TMN was put into 1 mL of Nafion/ethanol (0.25 wt % Nafion) solution through ultrasonic dispersion to form a slurry, and 4 μL of this slurry was pipetted onto a glassy carbon surface (5 mm inner diameter, 0.196 cm^{-2}) to function as a substrate. A mixture of $H_2PtCl_6{\cdot}6H_2O$ (5 mmol), polyvinylpyrrolidone (PVP, 50 mmol), 0.1 M Na_2SO_4, and 0.4 M H_2SO_4 solution was used as the electrolyte, and a PED procedure was applied to deposit a Pt layer on the surface of the TMN NPs. The T_{on} (time of connection) and T_{off} (time of disconnection) were 0.003 and 0.03 s, respectively. The theoretical deposited amount of Pt was calculated from the total deposition charge, and the actual Pt loading was determined using an inductively coupled plasma optical emission spectrometer (ICP-OES, Leeman PROFILE SPEC). The actual deposited amount was found to be about one-sixth of the theoretical deposited amount. Because no Pt NPs could be detected/observed by X-ray diffraction (XRD) and transmission electron microscopy (TEM), we denote the catalysts prepared in this work as TiNiN@Pt and TiN@Pt when TiNiN and TiN, respectively, were used as the substrates, although the catalysts may not have complete/perfect core−shell structures.

2.3. Physical Characterization of the Catalysts. XRD was conducted on a TD-3500 powder diffractometer (Tongda, China) operated at 30 kV and 20 mA, using Cu Kα radiation sources in a Bragg angle range of 20−86°. Energy dispersive X-ray analysis (EDX) was performed with a field-emission scanning electron microscope (FE-SEM, Hitachi S-4800). TEM and high-resolution transmission electron microscopy (HRTEM) images were acquired with a JEOL 2100 microscope. X-ray photoelectron spectroscopy (XPS) was performed on an Axis Ultra DLD X-ray photoelectron spectrometer employing a monochromated Al Kα X-ray source ($h\nu$ =1486.6 eV). The Brunauer−Emmett−Teller (BET) surface area and pore distribution were measured by nitrogen adsorption−desorption on a TristarII 3020 gas adsorption analyzer. High-angle annular dark field (HAADF) images and energy dispersive spectrometer (EDS) elemental mapping analysis were obtained using scanning transmission electron microscopy (STEM) mode on an aberration-corrected FEI Titan G2 60-300 field emission transmission electron microscope (FEI), operated at 300 kV (α_{max} = ∼100 mrad). Under these experimental conditions, the image contrast related directly to the atomic number (Z-contrast). The actual Pt loadings in this work were determined by analyzing the ICP-OES measurements.

2.4. Measurement of the Catalysts' Electrocatalytic Performance. All the electrochemical measurements were carried out on an electrochemical workstation (Ivium, Netherlands) at room temperature (25 ± 1 °C), using a three-electrode electrochemical setup with a rotating disk electrode (RDE) system (Pine Research Instrumentation). The cell consisted of a glassy carbon working electrode (GCE, 5 mm inner diameter, 0.196 cm^2), a platinum wire counter electrode, and an Ag/AgCl (saturated 3 M NaCl) reference electrode. All potentials in this work are quoted with respect to a reversible hydrogen electrode (RHE).

The catalyst electrode was prepared as follows. First, a catalyst ink was prepared by ultrasonicating a mixture of 5.0 mg of catalyst and 2 mL of Nafion (0.25 wt %) ethanol solution for 30 min. Subsequently, 8 mL of catalyst ink was pipetted onto the GCE surface. Finally, the GCE was dried under an infrared lamp for 5 min. The Pt loading was calculated from the Pt content in the Pt@TMN catalyst. For the JM Pt/C catalyst (3.3 nm, 20 wt % Pt supported on Vulcan XC-72R carbon), the Pt loading on the RDE was 5.61 μg cm^{-2}.

Cyclic voltammetry (CV) characterization of the catalysts in the absence of oxygen was typically carried out in the 0.1−1.3 V potential range at a scan rate of 50 mV s^{-1} in N_2-saturated 0.1 M $HClO_4$ solution. The ORR polarization curves were recorded in O_2-saturated 0.1 M $HClO_4$ electrolyte at a rotation rate of 1600 rpm and a scan rate of 10 mV s^{-1}. Accelerated durability testing (ADT) was performed in O_2-saturated 0.5 M H_2SO_4 solution in the 0.6−1.05 V potential range at room temperature.

3. RESULTS AND DISCUSSION

Figure 1 shows the powder XRD patterns of the as-prepared TiN and TiNiN NPs, respectively. The NPs exhibited the characteristic peaks of the face centered cubic (fcc) TiN phase (JCPDS No. 38−1420). After the high-temperature nitriding process, only the TiN phase (fcc) could be detected, suggesting that all the complex precursors had been converted to TiN nanostructures. For the TiNiN NPs, the locations of the diffraction peaks were almost identical to those of the TiN NPs, indicating that the Ni atoms entered the TiN lattice by substituting for the Ti atoms. However, an obvious peak shift was observable in the XRD patterns of TiNiN. Compression of the unit cell parameters may have occurred because Ni (0.056 nm) has a smaller ionic radius than Ti (0.067 nm). Notably, there were no signals corresponding to Ni metal, Ni oxides, or phase separation between Ti and Ni nitride, suggesting the effective incorporation of Ni into the TiN(fcc) structure to form a single-phase solid solution. The composition profile of

DOI: 10.1021/jacs.5b11364
J. Am. Chem. Soc. 2016, 138, 1575−1583

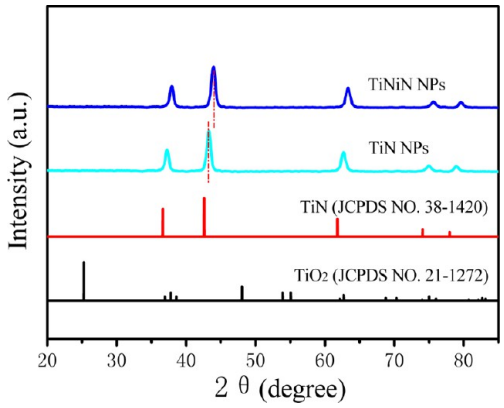

Figure 1. XRD patterns of as-prepared TiN and TiNiN NPs.

TiNiN demonstrated a Ti:Ni atomic ratio of 46.91:2.50,[43] which agrees well with the expected atomic ratio of 19:1 used in the precursors. This confirmed that our facile method is sound and that the composition of the binary TMNs can be controlled without using a template or surfactant.

TEM was used to discern the morphology of the TiN and TiNiN NPs. NP aggregation was observable (Figure 2), and the

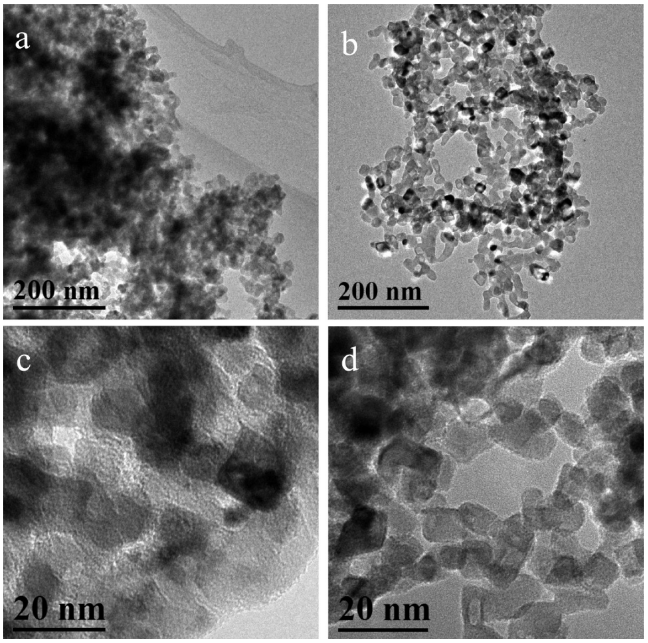

Figure 2. TEM images of (a,c) TiN and (b,d) TiNiN NPs.

TiN NPs exhibited a spherical nanostructure, whereas in the TiNiN material, some cubic morphologies were clearly evident (Figure 2d). The XRD results indicated that the crystallite sizes of TiN and TiNiN were ca. 9.8 and 9.2 nm, respectively, much smaller than those for previously reported free-standing TMN NPs.[44,45] Figure S1 presents the selected area electron diffraction (SAED) pattern of the TiN NPs; concentric rings composed of bright, discrete diffraction spots were observed and indexed to the (331), (400), (222),(311), (220), (200), and (111) crystal planes of the TiN (fcc) structure, demonstrating the high degree of crystallinity of individual TiN NPs.

The detailed structural features of the TiN and TiNiN NPs were determined using HRTEM, as shown in Figure S2. A well-defined crystalline lattice was observable, with a lattice spacing of 0.251 and 0.250 nm for TiN and TiNiN, respectively, corresponding to the (111) plane of TiN (fcc),[46] these figures are consistent with the XRD results.

Figure 3 presents TEM and HRTEM images of TiNiN@Pt, while images of TiN@Pt are presented in Figure S3. As can be

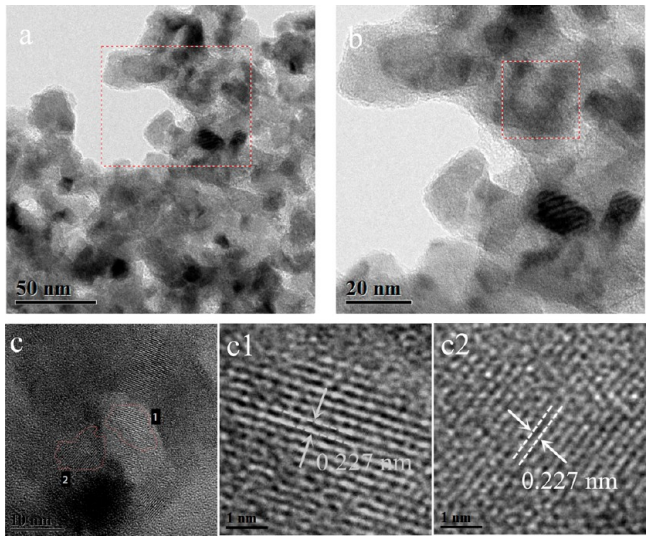

Figure 3. (a) TEM images of TiNiN@Pt catalyst; (b) enlarged TEM image of the area marked in (a); (c) enlarged TEM of the area marked in (b); (c1, c2) HRTEM images with high magnification of the areas marked in (c).

seen, no Pt NPs were observable in either of the samples. However, some lattice fringes were evident and corresponded to the interplane spacing of Pt (111) planes (0.227 nm),[47,48] suggesting that Pt existed on the surface of the nitrides as an ultrathin layer (i.e., several atoms thick).

Figure 4 shows the diffraction patterns of the TiN@Pt and TiNiN@Pt catalysts. All of the diffraction peaks were attributed

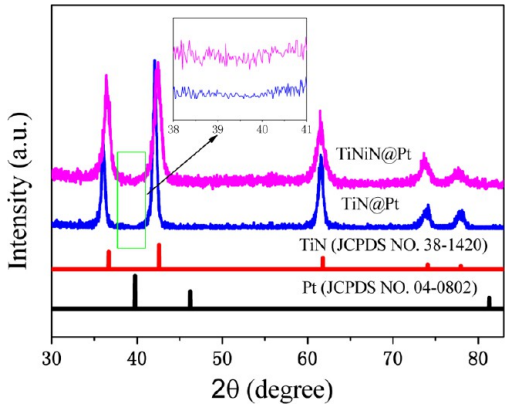

Figure 4. XRD patterns of TiN@Pt and TiNiN@Pt; the inset is an enlargement of the boxed area.

to the TiN (fcc) structure, and no separate diffraction peaks for Pt can be observed, indicating that there were no large, three-dimensional clusters (i.e., a few nanometers across) of the Pt single phases. The TEM-EDX profile (Figures S4 and S5) revealed that the average weight percentages of Pt in TiN@Pt and TiNiN@Pt were 5.09% and 4.98%, respectively. Furthermore, the overall Pt contents for TiN@Pt and

DOI: 10.1021/jacs.5b11364
J. Am. Chem. Soc. 2016, 138, 1575−1583

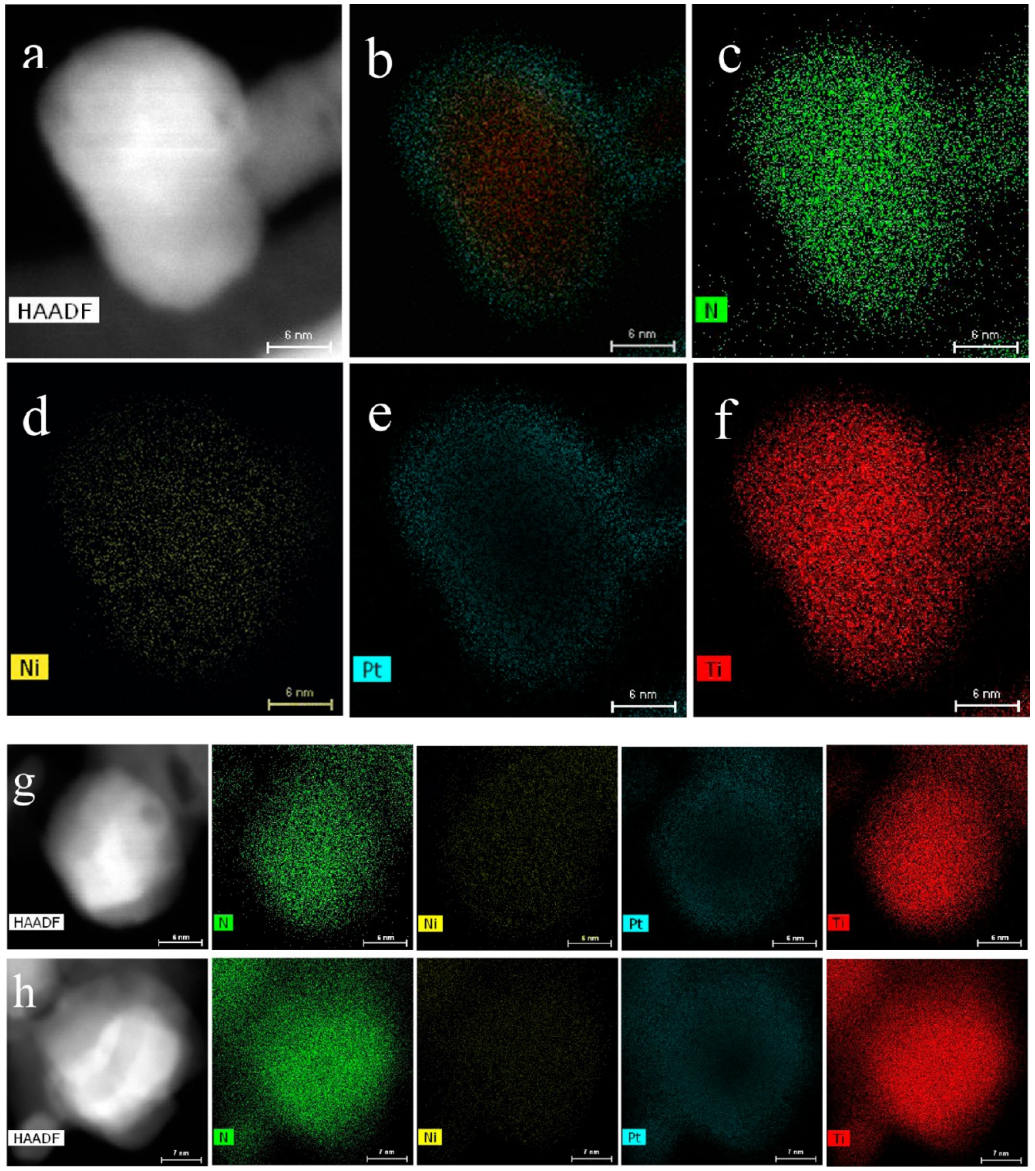

Figure 5. (a) HAADF/STEM image of a single TiNiN@Pt nanoparticle, and EDS elemental mapping of (c) N (green), (d) Ni (yellow), (e) Pt (blue), and (f) Ti (red) in the same area; (b) overlapping EDS elemental maps of Pt, N, Ni, and Ti; bar sizes = 6 nm; (g and h) two other particles and their elemental mapping images for N, Ni, Pt, and Ti; bar sizes = 6 and 7 nm, respectively.

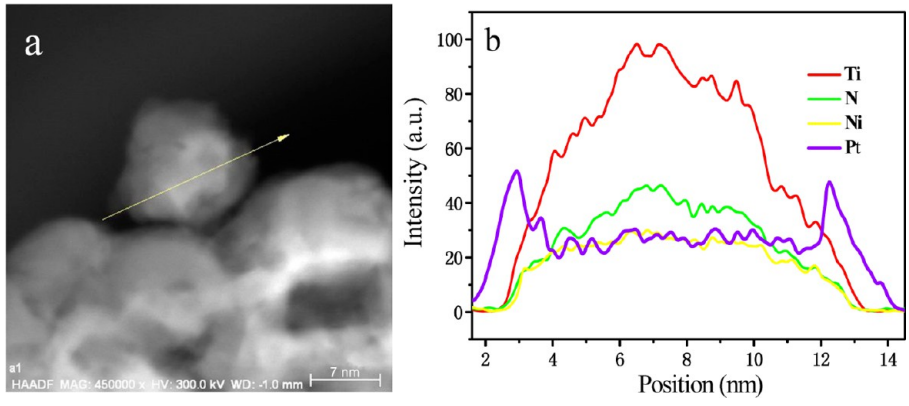

Figure 6. (a) HAADF/STEM image of a TiNiN@Pt nanoparticle. (b) Element distribution spectra obtained by EDS line-scanning analysis along the yellow arrow marked in (a).

DOI: 10.1021/jacs.5b11364
J. Am. Chem. Soc. 2016, 138, 1575−1583

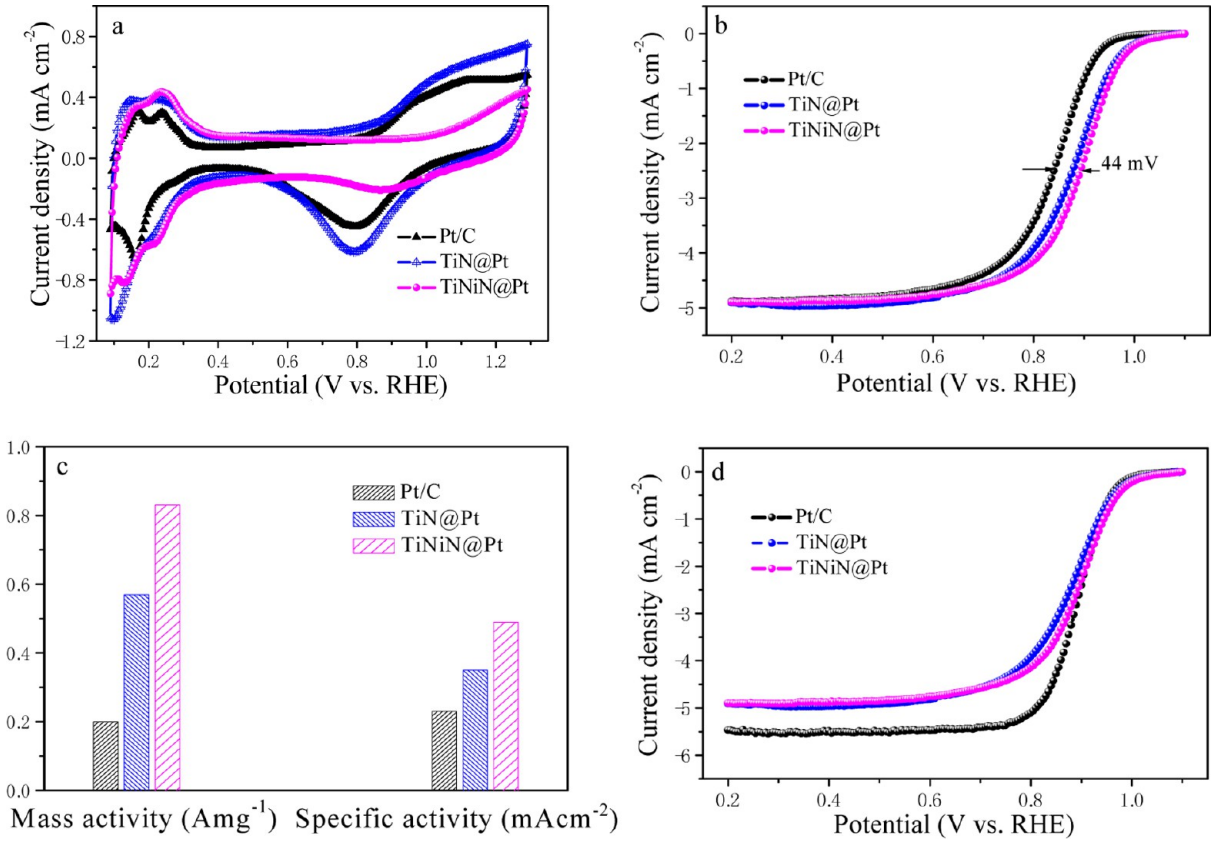

Figure 7. (a) CV curves of Pt/C, TiN@Pt, and TiNiN@Pt. (b and d) ORR polarization curves of the catalysts in 0.1 M $HClO_4$ solution saturated with O_2, using a RDE at 1600 rpm and a scan rate of 10 mV s^{-1}. (c) Pt mass activities and specific activities derived from (b) for the three catalysts. For the measurements in (a) and (b), the Pt loadings on a GC electrode for Pt/C, TiN@Pt, and TiNiN@Pt were 5.61, 5.53, and 5.44 μg cm^{-2}, respectively; for the measurements in (d), the Pt loading of Pt/C was increased to 20.36 μg cm^{-2}, but the Pt loadings of the other two catalysts were the same as in (b).

TiNiN@Pt were 5.15 and 5.06 wt %, corresponding to 5.53 and 5.44 μg cm^{-2}, respectively, as determined by ICP-OES, which agree well with the EDX results. If we consider the dispersion of Pt on the surface of the nitrides to have been uniform, the calculated thickness of the Pt layers was 0.11 nm, based on the specific surface area of the TiNiN NPs supported on the GCE. Therefore, the deposited Pt may have existed on the surface of the nitrides as either an ultrathin layer or amorphous NPs/layers. However, the obvious lattice fringes did not support the existence of the latter, so it is most probable that the Pt formed an ultrathin layer on the nitride NPs.

To investigate the compositional distributions of Pt and Ni in TiNiN@Pt, we carried out elemental mapping using EDS coupled with HAADF/STEM. Figure 5a shows the HAADF/STEM image of a single TiNiN@Pt NPs; the EDS elemental mapping of N (Figure 5c), Ni (Figure 5d), Pt (Figure 5e), and Ti (Figure 5f) is presented in the same region. The images revealed that these components in the NPs, along with the Ni atoms, were distributed uniformly with the N and Ti atoms. Figure 5b depicts the overlapping Pt, N, Ni, and Ti compositional distributions. The intensity of the Pt component is continuously distributed over the TiNiN NP, with one interesting feature: its density is slightly higher at the NP rims, demonstrating the formation of a core (TiNiN) and shell (Pt) structure. We also measured two other TiNiN@Pt NPs with EDS elemental mapping, and these results strongly confirmed the unique core−shell nanostructure of the catalyst particles (Figure 5g and h).

To further explore the structure of the catalyst, we carried out EDS line-scanning measurement on a typical TiNiN@Pt nanoparticle. Figure 6a shows the HAADF/STEM image of the nanoparticle, with the scanning path presented as a yellow arrow. From the scanning spectra of Pt, Ni, N, and Ti shown in Figure 6b, we can see that the Ti, Ni, and N signals emerged simultaneously, and the strongest signals appeared at the central position of the particle. However, Pt exhibited a different scanning spectrum, with a position difference from Ti and two symmetric peaks, confirming the core−shell structure of the TiNiN@Pt particle. In addition, from the position difference between the Pt and Ti signals, we determined the thickness of the Pt layer to be around 0.9 nm, corresponding to approximately 2−3 Pt atomic layers.

Figure 7a shows the CV curves of Pt/C, TiN@Pt, and TiNiN@Pt in N_2-saturated 0.5 M H_2SO_4 solution. The ECSA of the catalysts was obtained by calculating the charge using the hydrogen under potential desorption (H_{UPD}) area.[49] The calculated ECSAs of TiN@Pt and TiNiN@Pt were 94 and 97 m^2 g Pt^{-1}, respectively, both about 1.7 times that of the Pt/C catalyst (55.4 m^2 g Pt^{-1}). The larger ECSAs of Pt for TiN@Pt and TiNiN@Pt were most likely due to the high dispersion of Pt, which created a large Pt surface, further confirming that the Pt may have existed on the surface of the nitrides as an ultrathin layer. Figure 7b shows the polarization curves of Pt/C, TiN@Pt, and TiNiN@Pt in an O_2-saturated 0.1 M $HClO_4$ solution, using a RDE at 1600 rpm; the current density was normalized to the geometric surface area of the electrode. As

DOI: 10.1021/jacs.5b11364
J. Am. Chem. Soc. 2016, 138, 1575−1583

can be seen, TiN@Pt and TiNiN@Pt both showed better catalytic activity toward the ORR than the JM Pt/C catalyst with the same Pt loading. The half-wave potential measured from the ORR polarization curves for TiNiN@Pt was 893 mV, which was 16 and 44 mV higher than for TiN@Pt and Pt/C, respectively. To better understand the synthesized electrocatalysts' observed catalytic activities for the ORR, we calculated the mass activity and specific activity at 0.90 V based on the ORR polarization curves. The kinetic current was calculated from the ORR polarization curves using the Koutecky–Levich equation:[50] $1/i = 1/i_k + 1/i_d$ (where i_k is the kinetic current and i_d is the diffusion-limiting current). The mass activity was obtained by normalizing the kinetic current to the Pt loading, and the specific activity was determined by normalizing the kinetic current to the ECSA. Figure 7c compares the mass activities of Pt/C, TiN@Pt, and TiNiN@Pt; evidently, TiNiN@Pt exhibited a mass activity of 0.83 A mg^{-1}_{Pt}, which was four times greater than that of the Pt/C catalyst. At the same time, the specific activity of TiNiN@Pt was 0.49 mA cm^{-2}, which was also much higher than that of either Pt/C or TiN@Pt. Furthermore, the onset potential of TiNiN@Pt was positively shifted by 20 mV compared with the Pt/C catalyst, even though the former's Pt loading was only one-fourth of the latter's (Figure 7d). The Pt mass activity of our nitride-based core–shell catalyst was completely comparable to activities reported for most core–shell catalysts with precious metal cores (see Tables 1 and S1).

Table 1. Pt Mass Activities and Specific Activities of Some Typical Core–Shell Catalysts with Precious Metal NPs as the Core, and Our Nitride-Core Catalyst

sample	mass activity	specific activity	ref
$Pd@Pt_{1.8}Ni$	0.79	0.44	19
Ru@Pt	0.92	0.63	27
Pd@Pt	0.35	0.35	51
Pd@Pt	0.64	1.36	52
AuCu@Pt	0.56	0.37	53
Pd@Pt	1.60	1.66	54
TiNiN@Pt	0.83	0.49	this work

Compared with TiN@Pt, TiNiN@Pt displayed significantly better ORR activity, indicating that Ni doping had a positive effect toward the ORR activity. As shown in Figure 7a, TiNiN@Pt exhibited a much lower Pt oxidation current in the high potential region than JM Pt/C and TiN@Pt. The positive shift in Pt oxidation potential demonstrated weakened interactions between Pt and intermediate oxide species, caused by a down-shift in the d-band center of Pt.[49,55] It is also worth noting previous findings[37,56] that OH groups can be adsorbed on the surface of TiN, so a TiN or TiNiN support can lower the amount of potential OH coverage on supported Pt by inducing lateral repulsion between OH species on the Pt atoms and neighboring OH species adsorbed on the TiN/TiNiN NPs.[55,57−59] In principle, decreasing the OH coverage on Pt will reduce the overpotential for the ORR, and the weakened interaction between Pt and intermediate oxide species will introduce a balance between O–O bond breakage and the removal of surface oxides,[60,61] resulting in TiNiN@Pt having better ORR performance than TiN@Pt.

To understand the connection between Ni doping and the superior ORR catalytic activity of TiNiN@Pt, we collected the XPS spectra of Pt/C, TiN@Pt, and TiNiN@Pt (Figure 8).

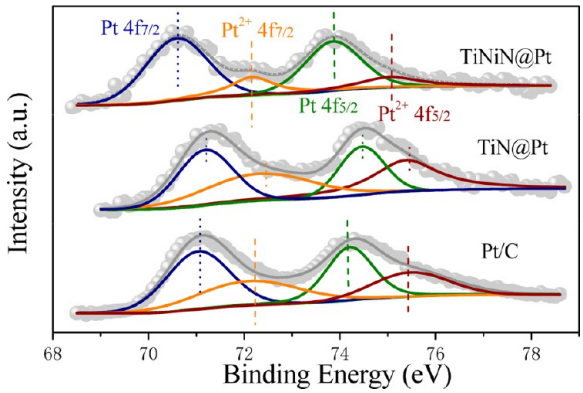

Figure 8. Pt 4f XPS spectra of Pt/C, TiN@Pt, and TiNiN@Pt.

Each Pt 4f peak can be deconvoluted into two pairs of doublets. According to the deconvolution results, a large proportion of the Pt atoms in the TiN@Pt catalyst existed as Pt (II), whereas in TiNiN@Pt they existed mainly as Pt (0). Comparing the relative integrated areas of the Pt (0) and Pt (II) peaks demonstrates that Ni doping significantly increased the atomic ratio of Pt (0) in TiNiN@Pt, which may have been one of the main reasons for its superb performance in comparison with TiN@Pt. In addition, the strong covalent interactions between Pt atoms and the core TiNiN NPs was evidenced by the clear shift in the Pt $4f_{7/2}$ peak to a lower binding energy, by 0.38 and 0.50 eV in comparison with commercial Pt/C and TiN@Pt, respectively. The negative shift implies that the Pt atoms obtained electrons from the doped Ni in the TiNiN NPs,[48,63] leading to a down-shift in the d-band center of Pt and suggesting that the electronic structure of Pt atoms can be modified by Ni doping. The strong metal–support interaction between the negatively charged Pt atoms and the TiNiN support helped to stabilize the Pt atoms on the TiNiN support.

It is notable that a slight positive shift of the Pt 4f7/2 binding energy relative to that of Pt/C was observable for TiN@Pt, implying that electron transfer may have occurred from Pt to Ti or N atoms. This might have been because there was a stronger interaction between the highly dispersed Pt and the titanium oxide/nitride in TiN@Pt than between the Pt NPs and the carbon support.[36,56,62]

The catalysts' stability/durability was evaluated by potential cycling between 0.6 and 1.05 V for 10 000 cycles in an O_2-saturated 0.5 M H_2SO_4 solution at a scan rate of 50 mV s^{-1}. The evolutions of the CV curves for Pt/C, TiN@Pt and TiNiN@Pt obtained after every 2000 cycles are shown in Figure 9a–c, respectively. The ECSA of Pt/C dropped almost 26% after the first 2000 cycles, and then the decay rate slowed with continued cycling; the final ECSA after 10 000 cycles had dropped to about 55% of the initial value. However, the TiN@Pt and TiNiN@Pt samples showed much better ECSA retention, with 67% and 79% of the initial ECSA remaining after 10 000 cycles (Figure 9d), respectively. We also investigated the catalysts' stability/durability toward the ORR. After 10,000 potential cycles in O_2-saturated $HClO_4$ electrolyte, Pt/C showed a degradation of more than 25 mV in its half-wave potential ($E_{1/2}$) (Figure 9e), whereas TiN@Pt and TiNiN@Pt degraded by only 17 and 10 mV, respectively. As shown in Figure 9f, TiN@Pt and TiNiN@Pt, especially the latter, exhibited much better stability/durability than commercial Pt/C in terms of both Pt mass and specific activity, making

DOI: 10.1021/jacs.5b11364
J. Am. Chem. Soc. 2016, 138, 1575–1583

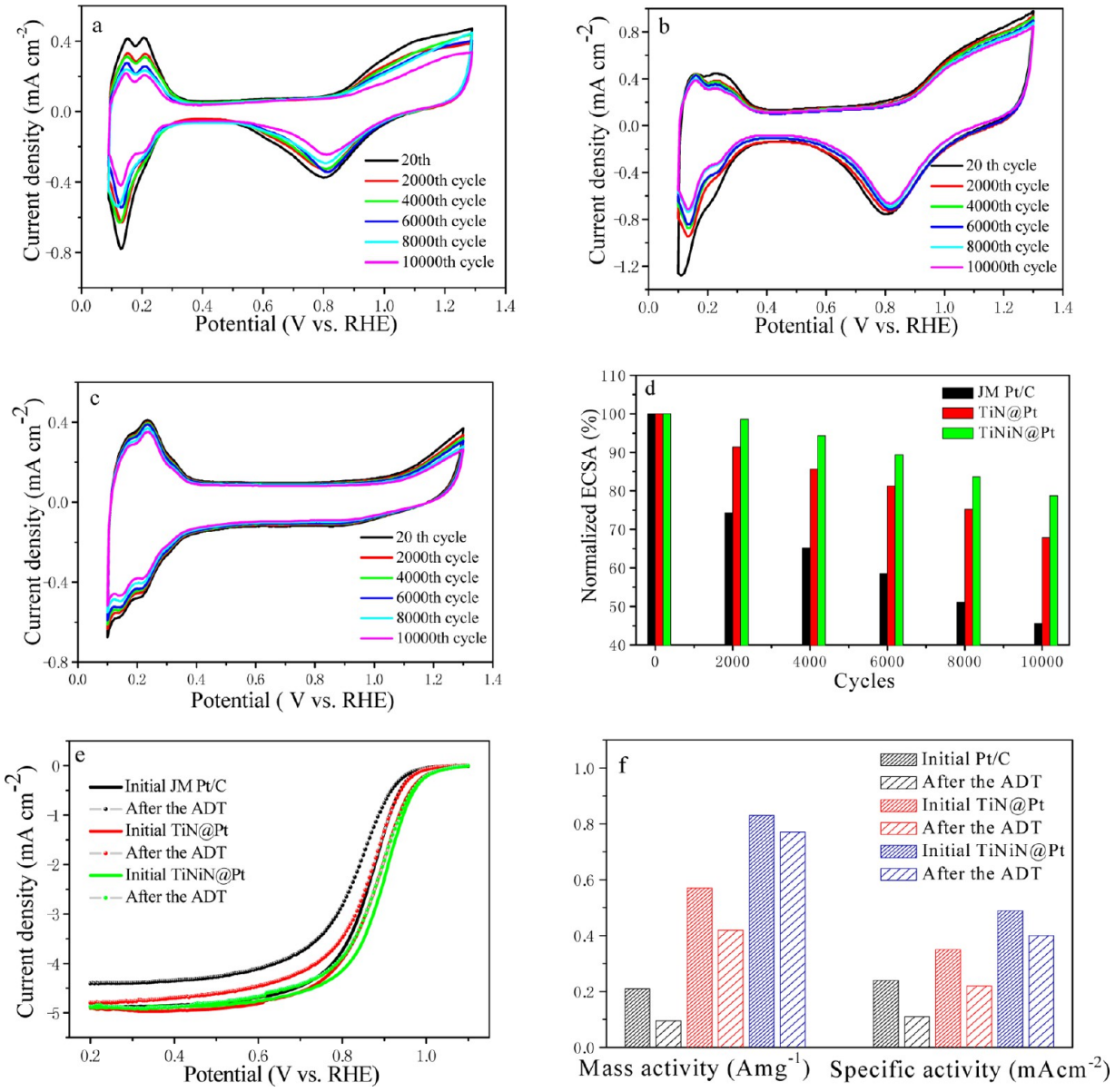

Figure 9. (a–c) Evolutions of CV curves after various numbers of cycles. (d) Comparison of ECSA loss. (e) Polarization curves of before (solid curves) and after (dashed curves) the ADT test. (f) Mass and specific activities of Pt/C, TiN@Pt, and TiNiN@Pt catalysts before and after the durability test.

our nitride-based catalysts promising for long-term PEMFC applications.

The excellent stability of TiNiN@Pt after 10 000 electrochemical cycles was also verified by the TEM images. As shown in Figure S6a–c, compared with the TEM images of TiNiN@Pt before potential cycling (Figure 3), although some coalesced and/or aggregated Pt nanoparticles were observable, the Pt layer and TiNiN structure had been preserved (Figure S6d,e). Furthermore, the EDS profile of TiNiN@Pt revealed only a slight Pt loss after the ADT (Figure S7). For Pt/C, however, the average Pt size increased from 3.2 to 8.7 nm (Figure S8), and a significant decrease in Pt density on the carbon support was observable after the ADT, implying that the major causes of ECSA and ORR performance loss in carbon support were Pt detachment and ripening issues related to carbon-support corrosion.[31,64] Although the exact nature of Pt stability in TiNiN@Pt is still not well understood, it is plausible to hypothesize that the strong Pt–TiNiN interaction alters the electronic structure of the Pt atoms, which shifts the Pt $4f_{7/2}$ peak to lower binding energies, thereby creating a stabilizing effect against Pt oxidation/dissolution. Thus, the oxidation of Pt atoms on TiNiN becomes more difficult than on the carbon support. This is confirmed by comparing the CV curves of the three catalysts, where a higher Pt oxidation potential is evident for TiNiN@Pt (Figure7a). Another possible reason is that nitrides have greater stability than carbon materials against oxidation/corrosion in harsh electrochemical conditions.[44,46] Future work will focus on further improving the long-term stability of TiNiN@Pt and fuel cell performance, using a TiNiN@Pt catalyst as the cathode will also be studied.

4. CONCLUSIONS

In conclusion, we have developed a robust, carbon-free TiNiN@Pt catalyst using a two-stage approach: preparing nitride nanoparticles with small particle sizes by nitriding a

DOI: 10.1021/jacs.5b11364
J. Am. Chem. Soc. 2016, 138, 1575–1583

transition metal ammonia complex, followed by depositing an ultrathin Pt layer on the nitride nanoparticles with a pulse deposition method. The catalyst exhibited outstanding ORR activity and stability. Compared with commercial Pt/C, with carbon as support and Pt being nanoparticles, our catalyst exhibited much higher Pt dispersion and utilization, as well as much greater stability, since it did not have carbon corrosion problems. In addition, our catalyst is not only much cheaper, but also avoids carbon-support corrosion issues even compared with carbon supported core−shell catalysts with precious metal NPs as the core. The addition of nickel significantly improved the catalyst's ORR performance, and we suggest that the considerable performance improvement was probably due to high Pt dispersion and utilization, the synergistic effect introduced by Ni doping, the excellent stability of nitrides, and the strong interaction between the Pt layer and the TiNiN support. Our approach may provide a novel pathway for developing low-cost, carbon-free, highly stable, low-platinum electrocatalysts for fuel cell applications.

■ ASSOCIATED CONTENT

Supporting Information

The Supporting Information is available free of charge on the ACS Publications website at DOI: 10.1021/jacs.5b11364.

Detailed characterization results, and additional electrochemical data (PDF)

■ AUTHOR INFORMATION

Corresponding Authors

*chsjliao@scut.edu.cn

*adzic@bnl.gov

Notes

The authors declare no competing financial interest.

■ ACKNOWLEDGMENTS

This work was supported by the National Natural Science Foundation of China (NSFC Project Nos. 21276098, 21476088, 51302091, U1301245), Natural Science Foundation of Guangdong Province (Project No. 2015A030312007), and Educational Commission of Guangdong Province (Project No. 2013CXZDA003).

■ REFERENCES

(1) Liu, Y.; Mustain, W. E. *J. Am. Chem. Soc.* **2013**, *135*, 530.

(2) Youn, D. H.; Bae, G.; Han, S.; Kim, J. Y.; Jang, J.-W.; Park, H.; Choi, S. H.; Lee, J. S. *J. Mater. Chem. A* **2013**, *1*, 8007.

(3) Peng, H.; Mo, Z.; Liao, S.; Liang, H.; Yang, L.; Luo, F.; Song, H.; Zhong, Y.; Zhang, B. *Sci. Rep.* **2013**, *3*, 1765.

(4) Peng, H.; Hou, S.; Dang, D.; Zhang, B.; Liu, F.; Zheng, R.; Luo, F.; Song, H.; Huang, P.; Liao, S. *Appl. Catal., B* **2014**, *158−159*, 60.

(5) Greeley, J.; Stephens, I. E. L.; Bondarenko, A. S.; Johansson, T. P.; Hansen, H. A.; Jaramillo, T. F.; Rossmeisl, J.; Chorkendorff, I.; Norskov, J. K. *Nat. Chem.* **2009**, *1*, 552.

(6) Stamenkovic, V. R.; Fowler, B.; Mun, B. S.; Wang, G.; Ross, P. N.; Lucas, C. A.; Markovic, N. M. *Science* **2007**, *315*, 493.

(7) Liao, S. J.; Holmes, K. A.; Tsaprailis, H.; Birss, V. I. *J. Am. Chem. Soc.* **2006**, *128*, 3504.

(8) Liang, Y.; Wang, H.; Diao, P.; Chang, W.; Hong, G.; Li, Y.; Gong, M.; Xie, L.; Zhou, J.; Wang, J.; Regier, T. Z.; Wei, F.; Dai, H. *J. Am. Chem. Soc.* **2012**, *134*, 15849.

(9) Stamenkovic, V. R.; Mun, B. S.; Mayrhofer, K. J. J.; Ross, P. N.; Markovic, N. M. *J. Am. Chem. Soc.* **2006**, *128*, 8813.

(10) Wang, D.; Xin, H. L.; Hovden, R.; Wang, H.; Yu, Y.; Muller, D. A.; DiSalvo, F. J.; Abruna, H. D. *Nat. Mater.* **2013**, *12*, 81.

(11) Strasser, P.; Koh, S.; Anniyev, T.; Greeley, J.; More, K.; Yu, C.; Liu, Z.; Kaya, S.; Nordlund, D.; Ogasawara, H.; Toney, M. F.; Nilsson, A. *Nat. Chem.* **2010**, *2*, 454.

(12) Ghosh, T.; Vukmirovic, M. B.; DiSalvo, F. J.; Adzic, R. R. *J. Am. Chem. Soc.* **2010**, *132*, 906.

(13) Adzic, R. R.; Zhang, J.; Sasaki, K.; Vukmirovic, M. B.; Shao, M.; Wang, J. X.; Nilekar, A. U.; Mavrikakis, M.; Valerio, J. A.; Uribe, F. *Top. Catal.* **2007**, *46*, 249.

(14) Sasaki, K.; Kuttiyiel, K. A.; Su, D.; Adzic, R. R. *Electrocatalysis* **2011**, *2*, 134.

(15) Wang, J. X.; Inada, H.; Wu, L. J.; Zhu, Y. M.; Choi, Y. M.; Liu, P.; Zhou, W. P.; Adzic, R. R. *J. Am. Chem. Soc.* **2009**, *131*, 17298.

(16) Xu, C.; Wang, R.; Chen, M.; Zhang, Y.; Ding, Y. *Phys. Chem. Chem. Phys.* **2010**, *12*, 239.

(17) Wang, D.; Yu, Y.; Xin, H. L.; Hovden, R.; Ercius, P.; Mundy, J. A.; Chen, H.; Richard, J. H.; Muller, D. A.; DiSalvo, F. J.; Abruna, H. D. *Nano Lett.* **2012**, *12*, 5230.

(18) Guo, S.; Zhang, S.; Su, D.; Sun, S. *J. Am. Chem. Soc.* **2013**, *135*, 13879.

(19) Zhao, X.; Chen, S.; Fang, Z.; Ding, J.; Sang, W.; Wang, Y.; Zhao, J.; Peng, Z.; Zeng, J. *J. Am. Chem. Soc.* **2015**, *137*, 2804.

(20) Sasaki, K.; Naohara, H.; Choi, Y.; Cai, Y.; Chen, W. F.; Liu, P.; Adzic, R. R. *Nat. Commun.* **2012**, *3*, 1115.

(21) Dang, D.; Zou, H.; Xiong, Z. a.; Hou, S.; Shu, T.; Nan, H.; Zeng, X.; Zeng, J.; Liao, S. *ACS Catal.* **2015**, *5*, 4318.

(22) Lu, X.; Luo, F.; Song, H.; Liao, S.; Li, H. *J. Power Sources* **2014**, *246*, 659.

(23) Kuttiyiel, K. A.; Sasaki, K.; Choi, Y.; Su, D.; Liu, P.; Adzic, R. R. *Energy Environ. Sci.* **2012**, *5*, 5297.

(24) Dang, D.; Liao, S.; Luo, F.; Hou, S.; Song, H.; Huang, P. *J. Power Sources* **2014**, *260*, 27.

(25) Chen, D.; Chen, R.; Dang, D.; Shu, T.; Peng, H.; Liao, S. *Electrochem. Commun.* **2014**, *46*, 115.

(26) Huang, M.; Dong, G.; Wang, N.; Xu, J.; Guan, L. *Energy Environ. Sci.* **2011**, *4*, 4513.

(27) Yang, L.; Vukmirovic, M. B.; Su, D.; Sasaki, K.; Herron, J. A.; Mavrikakis, M.; Liao, S.; Adzic, R. R. *J. Phys. Chem. C* **2013**, *117*, 1748.

(28) Xia, B. Y.; Ng, W. T.; Wu, H. B.; Wang, X.; Lou, X. W. *Angew. Chem., Int. Ed.* **2012**, *51*, 7213.

(29) Chen, S.; Wei, Z.; Qi, X.; Dong, L.; Guo, Y. G.; Wan, L.; Shao, Z.; Li, L. *J. Am. Chem. Soc.* **2012**, *134*, 13252.

(30) Yang, M.; Van Wassen, A. R.; Guarecuco, R.; Abruña, H. D.; DiSalvo, F. J. *Chem. Commun.* **2013**, *49*, 10853.

(31) He, D. P.; Mu, S. C.; Pan, M. *Carbon* **2011**, *49*, 82.

(32) Thanh Ho, V. T.; Pillai, K. C.; Chou, H.-L.; Pan, C.-J.; Rick, J.; Su, W.-N.; Hwang, B.-J.; Lee, J.-F.; Sheu, H.-S.; Chuang, W.-T. *Energy Environ. Sci.* **2011**, *4*, 4194.

(33) Wang, A.-L.; Xu, H.; Feng, J.-X.; Ding, L.-X.; Tong, Y.-X.; Li, G.-R. *J. Am. Chem. Soc.* **2013**, *135*, 10703.

(34) Kumar, R.; Pasupathi, S.; Pollet, B. G.; Scott, K. *Electrochim. Acta* **2013**, *109*, 365.

(35) Chen, J.; Takanabe, K.; Ohnishi, R.; Lu, D.; Okada, S.; Hatasawa, H.; Morioka, H.; Antonietti, M.; Kubota, J.; Domen, K. *Chem. Commun.* **2010**, *46*, 7492.

(36) Avasarala, B.; Murray, T.; Li, W.; Haldar, P. *J. Mater. Chem.* **2009**, *19*, 1803.

(37) Thotiyl, M. M. O.; Sampath, S. *Electrochim. Acta* **2011**, *56*, 3549.

(38) Yang, M.; Cui, Z.; DiSalvo, F. J. *Phys. Chem. Chem. Phys.* **2013**, *15*, 7041.

(39) Cui, Z.; Yang, M.; DiSalvo, F. J. *ACS Nano* **2014**, *8*, 6106.

(40) Cui, Z.; Burns, R. G.; DiSalvo, F. J. *Chem. Mater.* **2013**, *25*, 3782.

(41) Yang, M.; Guarecuco, R.; DiSalvo, F. J. *Chem. Mater.* **2013**, *25*, 1783.

(42) Chen, D.; Li, Y.; Liao, S.; Su, D.; Song, H.; Li, Y.; Yang, L.; Li, C. *Sci. Rep.* **2015**, *5*, 11604.

(43) Tian, X.; Luo, J.; Nan, H.; Fu, Z.; Zeng, J.; Liao, S. *J. Mater. Chem. A* **2015**, *3*, 16801.

(44) Yang, M.; Cui, Z.; DiSalvo, F. J. *Phys. Chem. Chem. Phys.* **2013**, *15*, 1088.

DOI: 10.1021/jacs.5b11364
J. Am. Chem. Soc. 2016, 138, 1575−1583

(45) Yang, M. H.; DiSalvo, F. J. *Chem. Mater.* **2012**, *24*, 4406.
(46) Dong, Y.; Wu, Y.; Liu, M.; Li, J. *ChemSusChem* **2013**, *6*, 2016.
(47) Li, Y.; Li, Y.; Zhu, E.; McLouth, T.; Chiu, C. Y.; Huang, X.; Huang, Y. *J. Am. Chem. Soc.* **2012**, *134*, 12326.
(48) Ho, V. T.; Pan, C. J.; Rick, J.; Su, W. N.; Hwang, B. J. *J. Am. Chem. Soc.* **2011**, *133*, 11716.
(49) Kuttiyiel, K. A.; Sasaki, K.; Choi, Y.; Su, D.; Liu, P.; Adzic, R. R. *Nano Lett.* **2012**, *12*, 6266.
(50) Hsu, S. P.; Liu, C. W.; Chen, H. S.; Chen, T. Y.; Lai, C. M.; Lee, C. H.; Lee, J. F.; Chan, T. S.; Tsai, L. D.; Wang, K. W. *Electrochim. Acta* **2013**, *105*, 180.
(51) Xie, S.; Choi, S. I.; Lu, N.; Roling, L. T.; Herron, J. A.; Zhang, L.; Park, J.; Wang, J.; Kim, M. J.; Xie, Z.; Mavrikakis, M.; Xia, Y. *Nano Lett.* **2014**, *14*, 3570.
(52) Wang, X.; Choi, S. I.; Roling, L. T.; Luo, M.; Ma, C.; Zhang, L.; Chi, M.; Liu, J.; Xie, Z.; Herron, J. A.; Mavrikakis, M.; Xia, Y. *Nat. Commun.* **2015**, *6*, 7594.
(53) Wang, G.; Huang, B.; Xiao, L.; Ren, Z.; Chen, H.; Wang, D.; Abruna, H. D.; Lu, J.; Zhuang, L. *J. Am. Chem. Soc.* **2014**, *136*, 9643.
(54) Wang, X.; Vara, M.; Luo, M.; Huang, H.; Ruditskiy, A.; Park, J.; Bao, S.; Liu, J.; Howe, J.; Chi, M.; Xie, Z.; Xia, Y. *J. Am. Chem. Soc.* **2015**, *137*, 15036.
(55) Liu, H.; Koenigsmann, C.; Adzic, R. R.; Wong, S. S. *ACS Catal.* **2014**, *4*, 2544.
(56) Ottakam Thotiyl, M. M.; Ravikumar, T.; Sampath, S. *J. Mater. Chem.* **2010**, *20*, 10643.
(57) Nilekar, A. U.; Xu, Y.; Zhang, J.; Vukmirovic, M. B.; Sasaki, K.; Adzic, R. R.; Mavrikakis, M. *Top. Catal.* **2007**, *46*, 276.
(58) Huang, K.; Sasaki, K.; Adzic, R. R.; Xing, Y. *J. Mater. Chem.* **2012**, *22*, 16824.
(59) Huang, K.; Li, Y.; Yan, L.; Xing, Y. *RSC Adv.* **2014**, *4*, 9701.
(60) Stamenkovic, V.; Mun, B. S.; Mayrhofer, K. J. J.; Ross, P. N.; Markovic, N. M.; Rossmeisl, J.; Greeley, J.; Nørskov, J. K. *Angew. Chem.* **2006**, *118*, 2963.
(61) Lima, F. H. B.; Zhang, J.; Shao, M. H.; Sasaki, K.; Vukmirovic, M. B.; Ticianelli, E. A.; Adzic, R. R. *J. Phys. Chem. C* **2007**, *111*, 404.
(62) Higgins, D. C.; Choi, J.-Y.; Wu, J.; Lopez, A.; Chen, Z. *J. Mater. Chem.* **2012**, *22*, 3727.
(63) Wang, C.; Daimon, H.; Sun, S. H. *Nano Lett.* **2009**, *9*, 1493.
(64) Huang, S.-Y.; Ganesan, P.; Popov, B. N. *ACS Catal.* **2012**, *2*, 825.

DOI: 10.1021/jacs.5b11364
J. Am. Chem. Soc. 2016, 138, 1575−1583